Label-free optical fingerprints of hyperoxia-induced lung alterations in preterm rabbits

Respiratory Research

https://doi.org/10.1186/s12931-026-03583-9

Article in Press

Label-free optical fingerprints of hyperoxia-induced lung alterations in preterm rabbits

Received: 28 July 2025

Accepted: 14 February 2026

Published online: 25 February 2026

Cite this article as: Marazzini M., Scalera E., De Meo S. *et al.* Label-free optical fingerprints of hyperoxia-induced lung alterations in preterm rabbits. *Respir Res* (2026). https://doi.org/10.1186/s12931-026-03583-9

Margherita Marazzini, Enrica Scalera, Simone De Meo, Francesca Ricci, Gino Villetti, Xabier Murgia, Matteo Zoboli, Ferdinando Gazza, Gianmarco Ferri & Francesco Cardarelli

Title:

Label-Free Optical Fingerprints of Hyperoxia-Induced Lung Alterations in Preterm Rabbits

Authors:

Margherita Marazzini[1*], Enrica Scalera[2*], Simone De Meo[3], Francesca Ricci[2], Gino Villetti[2], Xabier Murgia[4], Matteo Zoboli[5], Ferdinando Gazza[5], Gianmarco Ferri[6], Francesco Cardarelli[1*]

Affiliations:

[1]NEST Laboratory-Scuola Normale Superiore, Pisa, Italy

[2]Department of Experimental Pharmacology and Translational Science, R&D, Chiesi Farmaceutici S.p.A., Parma, Italy.

[3]Department of Life Sciences, University of Siena, Siena

[4]Scientific Consultancy, Bilbao, Spain.

[5]Department of Veterinary Science, University of Parma, Parma Italy.

[6]Fondazione Pisana per la Scienza ONLUS, Pisa, Italy.

***Corresponding authors**

Correspondence to Francesco Cardarelli (francesco.cardarelli@sns.it) or Enrica Scalera (e.scalera@chiesi.com) or Margherita Marazzini (margherita.marazzini@sns.it)

Abstract

Background

Bronchopulmonary dysplasia (BPD) is a chronic lung disease of preterm neonates that carries significant long-term implications for respiratory health. Its pathogenesis is multifactorial, with oxygen toxicity and injury from mechanical ventilation being key contributing factors. While neonatal animal models exposed to hyperoxia are widely used to mimic human BPD, lung development is often assessed through classical histological analyses. Although these methods remain fundamental in preclinical study, they may require multiple staining techniques and sections to highlight key features of BPD. Here, we introduce a label-free, multi-modal imaging platform combining two-photon excitation fluorescence (TPEF), second harmonic generation (SHG), and fluorescence lifetime imaging microscopy (FLIM) to characterize the lung alterations induced by a 7-day hyperoxia (95% O_2) exposure in preterm rabbits.

Methods

Lung sections were obtained from preterm rabbit pups delivered at 28 gestational age (GA) (term 31 GA) either exposed to normoxia (21% O_2) or hyperoxia (95% O_2) for seven days. Lung sections were scanned with TPEF microscope at 780 nm and tissue intrinsic signals including autofluorescence intensity and lifetime, as well as SHG from collagen were simultaneously collected in the 470-570 nm, 420-460 nm and 380-410 nm ranges, respectively. BPD-relevant features were extracted from images, validated through traditional staining and immunolabelling and analyzed using an optimized pipeline. The tool reliability was tested by correlating label-free features with conventional Hematoxylin and eosin (H&E)-derived histomorphological parameters and lung functions measurements.

Results

This method simultaneously resolves key BPD-related features, such as tissue density (TD%), alveolar exudates, collagen deposition, arterial medial thickness (MT%) alterations, and alveolar

simplification, capturing the differences between hyperoxia and normoxia samples without dyes or antibodies. Quantitative outputs from our label-free pipeline strongly correlate with conventional histology and lung function measurements, thus validating its robustness.

Conclusion

This approach holds promise as a powerful tool for preclinical research, enabling simultaneous imaging and quantification of multiple pathological features with a single acquisition. This tool is envisioned to be integrated with classical histology and immunolabelling for a more comprehensive and information rich assessment of tissue alterations.

Keywords

Bronchopulmonary dysplasia (BPD); preterm rabbit; Hyperoxia; Label-free; Two-photon excitation fluorescence (TPEF); Second harmonic generation (SHG); Fluorescence lifetime imaging microscopy (FLIM)

Background

Bronchopulmonary dysplasia (BPD) is a chronic lung disease that primarily affects preterm infants born before 28 weeks of gestation (1). At this stage, the lungs are structurally immature, lacking fully developed alveoli and a functional surfactant system, both essential for extrauterine breathing (1,2). Despite advances in neonatal care, such as antenatal steroids, surfactant therapy, caffeine, and non-invasive ventilation strategies, BPD remains the most prevalent complication of prematurity (3) with long-term adverse consequences (4,5).

Animal models play a crucial role in evaluating preventive and therapeutic interventions. Large animal models, such as lambs and primates, closely mimic human BPD due to similar intrauterine lung development and the ability to be ventilated at birth. However, their use is limited by small litter sizes, high costs, and ethical concerns (6). Rodents' models have been widely used in the context of BPD (7–9), and although they circumvent many of the limitations of large animal models, they differ

from humans in key aspects of lung development. For instance, rodents are naturally delivered at the saccular stage of lung development with fully functional lungs, and unlike humans, alveolarization in rodents begins postnatally rather than prenatally (6).

The rabbit model has emerged as a valuable alternative, combining the practical advantages of small animal models with a lung developmental timeline that more closely resembles that of humans (6). Moreover, rabbits can be extracted prematurely at the saccular phase (10), thereby modeling prematurity, one of the primary risk factors for BPD (9). Indeed, the preterm rabbit model has been previously used to study hyperoxia-induced lung injury (6,10–14). A 7-day hyperoxia (95% O_2) exposure effectively generates histopathological features of human BPD, including impaired alveolar and vascular development, inflammation, and extracellular matrix (ECM) remodeling (9).

The main outcomes of preclinical studies in the context of BPD primarily derive from conventional analyses on chemically stained or immunolabeled histological lung preparations (15,16). For instance, alveolarization is usually assessed by calculating the radial alveolar count (RAC) from Hematoxylin and eosin (H&E)-stained lung sections, while the lung vasculature and pulmonary fibrosis have been assessed using H&E or Miller's elastic stain and Picrosirius Red (PSR) staining, respectively (6,11,13,17,18). Consequently, these approaches often require multiple staining techniques to visualize BPD relevant features. Moreover, immunolabeling may be particularly challenging in rabbit and lamb models due to the limited availability of antibodies for these species (9). Additionally, some stains and antibodies exhibit low specificity or poor contrast, which may compromise the accuracy of quantitative assessments.

Here we applied a multi-channel imaging approach to unlabeled histological lung sections of preterm rabbits exposed to either hyperoxia (95% O_2) or normoxia (21% O_2) for seven days. Combining two-photon excitation fluorescence (TPEF), second harmonic generation (SHG), and fluorescence lifetime imaging microscopy (FLIM), we were able to simultaneously capture high-resolution images

of alveolar and vascular structures, along with both qualitative and quantitative data on tissue density (TD) and collagen deposition. Our method effectively distinguished between normoxia and hyperoxia-exposed lungs, revealing hallmark features of BPD, including increased TD%, collagen accumulation, increased arterial medial thickness (MT%), and reduced alveolar density. Additionally, it showed a decrease in tissue autofluorescence intensity and increase in lifetime. This technique offers a non-destructive, label-free integrative approach for lung tissue analysis in the context of BPD. With further optimization and automation, this method holds significant potential for a broad range of applications in the histopathological analysis of preclinical and clinical research.

Materials and Methods

Experimental pipeline

The experimental pipeline, as illustrated in **Figure 1**, consists of two main phases, that we named "tool development" (**Figure 1a-d**) and "tool application" (**Figure 1e-f**). The "tool development" phase involves four steps: first, we collected lung sections from a well-established BPD model, specifically the preterm rabbit delivered at 28 gestational age (GA) and exposed either to 21% O_2 (Normoxia) or to 95% O_2 (Hyperoxia) for 7 days (**Figure 1a**). Notably, this step can also be considered part of the application phase, since a subset of both normoxic and hyperoxic tissue sections was used during the development phase, while sections from all n=6 normoxic and n=6 hyperoxic rabbits were used in the application phase. Second, we designed a multi-channel acquisition system to enable simultaneous visualization of lung parenchymal features by detecting tissue autofluorescence intensity, autofluorescence lifetime, and SHG upon TPEF (**Figure 1b**). Third, we extracted the label-free features and qualitatively validated them by performing standard staining or immunolabeling on some of the normoxia and hyperoxia sections previously acquired label-free (**Figure 1c**). H&E-staining was used to confirm the correspondence between autofluorescence signals and parenchymal structure, PSR staining to verify collagen identified via SHG, and immunolabelling with antibody against alfa smooth muscles actin (α-SMA) for confirming muscularized vascular

identification. Finally, for each feature, we optimized a protocol for analysis and quantification (**Figure 1d**). The "tool application" phase began by statistically comparing the behavior of each feature between all normoxia and hyperoxia samples to assess the tool's reliability in detecting hyperoxia-induced changes (**Figure 1e**). In the final step, we evaluated the robustness of the tool's analysis and outcomes by correlating the quantified label-free imaging features with the corresponding histological parameters derived from H&E-stained sections of the same animals. We further correlated the severity of histological alterations for each animal in both conditions with the corresponding impairments in lung function.

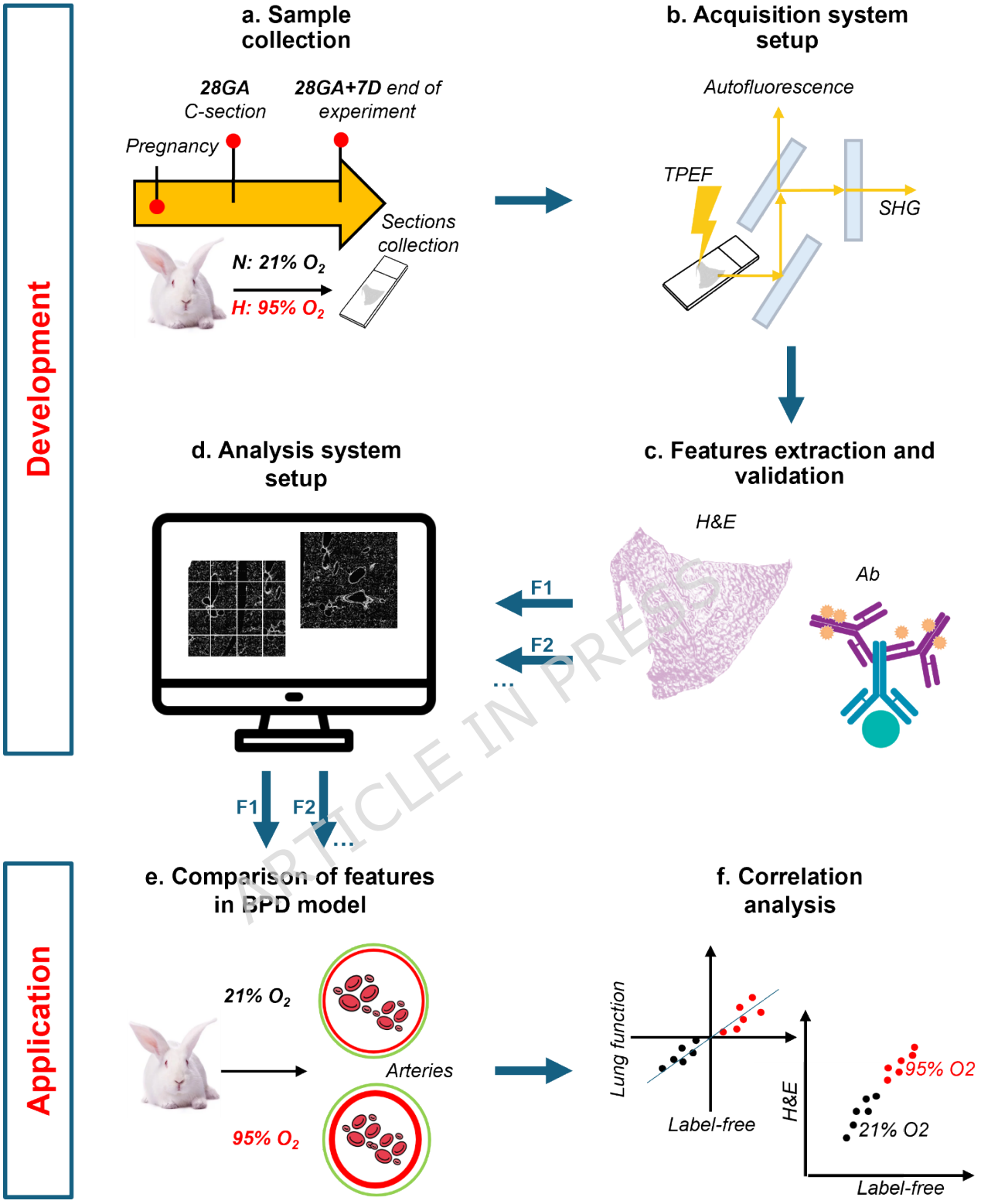

Figure 1. Experimental pipeline. The experimental approach consists of two main phases: the development of a quantitative label-free tool **(a-d)** and its application **(e-f)** to study hyperoxia-induced histological changes in a preterm rabbit model. **(a)** Lung sections were collected from rabbits delivered at 28 GA and either exposed for 7 days (7D) to normoxia ("N": 21% O_2) or hyperoxia ("H": 95% O_2). **(b)** Design of a multichannel imaging system to enable the

simultaneous visualization of BPD-relevant lung parenchymal features by detecting tissue autofluorescence intensity and lifetime, as well as SHG upon TPEF. **(c)** Extraction and validation of each label-free features ("F1", "F2" etc.) by using standard staining or immunolabelling ("Ab"). **(d)** Optimization of the analysis procedure for each feature ("F1", "F2" etc.). **(e)** Investigation of one feature ("F1", "F2" etc.) at a time to explore the differences between normoxia and hyperoxia in preterm rabbits. **(f)** Evaluating the robustness of the tool's analysis and findings by correlating the label-free features with corresponding measurements from H&E-stained sections, and by comparing the severity of histological changes with the severity of lung function impairments.

Animal care, delivery and experimental groups

All animal experiments were approved by the local animal ethics committee (Animal Welfare Body: Organismo Preposto al Benessere Animale [Italy], file number n°783/2019-PR), in accordance with European regulations for animal care. All the animal procedures were conducted at Chiesi Farmaceutici, an AAALAC accredited facility.

Timed pregnant New Zealand White rabbits were obtained from Charles River Laboratories (Domaine des Oncins, France) and maintained at 15–21 °C, relative humidity of 55% ± 15, 12:12 h light/dark cycles, and food and water *ad libitum* until the Caesarian section (C-section). C-sections were performed at 28 GA (term at 31 GA) (saccular stage) following the protocol described in detail elsewhere (14). Preterm pups were randomly assigned to two groups: normoxia (N=6), maintained at 21% oxygen for seven days, and hyperoxia (N=6) exposed to 95% oxygen for seven days to mimic the BPD phenotype. Oxygen exposure was conducted using custom-made incubators (Okolab, Italy). Pups were fed twice daily until postnatal day (PND) 7 with the formula described in detail elsewhere (14).

Lung function measurements

At PND7 lung function testing was performed using the forced oscillation technique with the flexiVent™ apparatus equipped with module 2 (SCIREQ, Canada), (module 2 for pups < 80gr). Preterm rabbits were initially anesthetized with ketamine (35 mg/kg) and xylazine (5 mg/kg) administered intramuscularly (i.m.). Then, a tracheostomy was performed with a 14-gauge metal

needle, and pups were connected to the volume-controlled mechanical ventilation of the flexiVent™ (tidal volume [V_T] 10 mL/kg, breath rate [BR] 120 breaths/min, positive end-expiratory pressure [PEEP] of 3 cmH_2O). Inspiratory capacity (IC), lung tissue damping (tissue resistance, G), lung tissue elastance (H), and static compliance (C_{st}) were determined. G and H were measured using the Primewave-8 forced oscillation, whereas C_{st} was determined using the pressure-volume curve. All measurements were performed until three consistent measurements were obtained, with a coefficient of determination > 0.95 as the limit to accept the measurement. The average of three measurements was calculated and used in the analysis.

Lung section collection

At PND7 pups were euthanized by an overdose of sodium pentothal prior to lungs harvesting. Then, the fixation procedure was performed ex-vivo following the protocol described elsewhere (13,14,19). Briefly, the lungs were removed *en bloc*, and a 14-gauge catheter was secured inside the trachea. The lungs were fixed with 10% buffered formalin (Sigma-Aldrich, Germany) for at least 4 h under constant pressure (25 cmH_2O). After that, the lungs were left in formalin for at least 24 h and then dehydrated in graded alcohol solutions, xylene clarified, and paraffin embedded. Dorsal serial sections 5 μm thick were selected at the same cutting depth for each animal using a rotary microtome.

Lung tissue histomorphometry

Lung sections collected from PND7 pups were stained with H&E according to the manufacturer's specifications (Histo-Line Laboratories). Histological slides were acquired as whole slide images by digital slide scanner (Nanozoomer S-60, Hamamatsu, Japan). The histomorphometrical analyses were performed on these slides, including RAC, MT%, and acute lung injury (ALI) score. RAC was determined by drawing a perpendicular line from the lumen of the terminal bronchiole to the nearest connective tissue septum or pleural margin and counting the number of saccules or alveoli intersected along this line (20,21). For MT% evaluation, 10 random peripheric muscularized vessels with external diameter (ED) <100 μm, corresponding in rabbits to the pre- and intra-acinar arteries, were

selected per section (13). MT% was calculated by measuring the external (ED) and internal (ID) short-side diameters and applying the following formula (22):

$$MT\% = \frac{(ED - ID)}{ED}$$

This proportional parameter accounts for variations due to vasodilation, vasoconstriction, and tissue shrinkage (22). The ALI score was assessed using the method proposed by the American Thoracic Society (23) and following the procedure outlined in (14). The method is based on five histological findings (i.e., neutrophils in the alveolar space, neutrophils in the interstitial space, hyaline membranes, proteinaceous debris in the airspace, and alveolar septal thickening).

For collagen evaluation, lung sections were stained with PSR and imaged using either brightfield microscopy or two-photon microscopy for fluorescence detection. PSR fluorescence has been shown to provide a stronger, collagen-specific signal compared to brightfield microscopy and, unlike linear polarized light microscopy, is insensitive to sample orientation (24,25). PSR-fluorescence staining was performed following the protocol described in detail elsewhere (25). Briefly, slides were incubated for 1 hour in a PSR staining solution containing 0.5 g of Direct Red 80 (Cat. 2610-10-8, Sigma-Aldrich Corp., St. Louis, MO) dissolved in 500 mL of saturated picric acid (Cat. P6744-1GA, Sigma-Aldrich Corp., St. Louis, MO). Slides were then washed twice with acidified water (0.5% acetic acid) and sequentially dehydrated through graded ethanol (EtOH) solutions (70%, 90%, 95%, and 100%). Residual EtOH was removed by two washes in xylene. Imaging was performed using a DPX mounting media (Thermo Scientific™). Lung sections were excited with TPEF at 1000 nm, and PSR signals were collected in the 505–680 nm range.

Immunohistochemistry

Immunohistochemistry was carried out by using a fully automated research stainer (Leica BOND RX, Leica Biosystems). The BOND Intense R Detection System (DS9263) was used for the visualization of immunostaining. It is a peroxidase-based detection system optimized to be used on the automated

stainer (BOND), and it contains peroxide block, streptavidin conjugated to horseradish peroxidase (HRP), 3,3'-diaminobenzidine (DAB) as chromogen and hematoxylin. Before staining, lung sections were deparaffinized through incubation with BOND Dewax Solution (AR9222) at 72°C and rehydrated in EtOH. Heat induced-antigen retrieval was performed by applying citrate-based pH 6.0 buffer at 95° C for 20 minutes (Epitope Retrieval 1-ER 1) (AR9961). Lung sections were incubated for 10 minutes with peroxide block (Leica Biosystems) and then 60 minutes with goat serum diluted 1:10 with PBS + Triton X-100 to block endogenous peroxidase and secondary antibody unspecific binding, respectively. Afterwards, lung sections were incubated for 1 hour with the primary antibody mouse monoclonal to Collagen Type I Alpha 1 Chain (Col1a1) (MA1-26671) at room temperature in dilution 1:500 with goat serum. For the detection of Col1a1, lung slices were incubated for 30 min with biotinylated goat anti-mouse BP-9200-500. Then, streptavidin, a biotin binding-protein, covalently conjugated to HRP enzyme (Leica Biosystems) was incubated for 30 minutes on each lung sample. The reaction was visualized by using DAB as chromogen.

Tissue deparaffinization and rehydration

For label-free imaging and immunofluorescence, paraffin was removed by immersing the collected 5 µm-thick lung sections in xylene (Cat. 534056-4L, Sigma-Aldrich) for three washes of ten minutes each. Residual xylene was eliminated by sequential immersion of the slides in EtOH solutions: three washes in 100% EtOH, followed by one wash in 95% EtOH and one wash in 70% EtOH, each for five minutes. EtOH was then removed by multiple washes in PBS. Lung sections were maintained in PBS until imaging.

Immunofluorescence

An optimized procedure and acquisition setting were developed for each antibody used. For Alfa-SMA (Goat polyclonal alpha smooth muscle actin, Abcam, ab21027) immunofluorescence, a buffer of 25mM Tris(hydroxymethyl)aminomethane hydrochloride (TRIS-HCL) pH 8,5, 1mM Ethylenediaminetetraacetic acid (EDTA), 0,05% Sodium dodecyl sulfate (SDS) was chosen for

antigen retrieval; Slides were immersed in this buffer for 10 min at 95 °C, then allowed to cool at room temperature (RT) for 30 min and washed 3 times in distilled H_2O. Samples were then permeabilized in 0.1% TritonX-100 in PBS (PBST) for 30-45 min at RT. After permeabilization, slides were incubated overnight (ON) at 4°C with a solution of 1:200 primary antibodies in PBST. After 3 washes for 10 min each at 37 °C with PBST, lung slices were incubated 1 h RT with a solution 1:1000 secondary antibodies (Alexa fluor 488 chicken anti-goat A-21467) in PBST. Three washes were then performed to remove unbound secondary antibody. The immunolabelled lung sections were acquired using two-photon microscope by exciting at 760 nm and the signals collected in the 380 – 570 nm. For Cluster of differentiation 31 (CD31) immunofluorescence (mouse monoclonal CD31/PECAM-1 [H-3], sc-376764), a buffer of 0.01 M pH 6.0 citrate was chosen for antigen retrieval. Slides were immersed in this buffer for 5 cycles of 5 min each in a microwave at 750 W and allowed to cool for 30 min. Slides were washed in PBS and immersed for 1 h with a blocking solution 3% Bovine Serum Albumin (BSA) in PBS. After the blocking step, slides were incubated ON at 4°C with a solution of 1:600 primary antibodies in BSA 3%. The following day, after the PBS washing steps, lung slices were incubated 1h at RT with a 1:1000 solution of the secondary antibody (Alexa fluor 555 donkey anti-mouse A322773) in BSA 3%. After washing and 5 min blocking in H_20, slides were incubated with the nuclear staining 4',6-diamidino-2-phenylindole (DAPI). Another washing step was performed before imaging. The stained lung sections were acquired with confocal microscope Stellaris 8 (Leica Microsystem, Germany) by exciting DAPI at 405 nm and collecting the signal between 425 and 470 nm, and by exciting the Alexa-555 secondary antibody linked to CD31 primary antibody at 553 nm and collecting the signal between 560 and 700 nm.

Two-photon and Fluorescence lifetime imaging microscopy

Lung sections were imaged using an Olympus FVMPE-RS microscope equipped with a two-photon Ti:sapphire laser (MaiTai HP, SpectraPhysics) operating at an 80-MHz repetition rate and a FLIMbox system (ISS, Urbana Champaign). Intrinsic tissue fluorescence and SHG signals from collagen were

induced by excitation at 780 nm. Emission signals were collected using a ×30 PlanApo silicon immersion objective (Numerical aperture = 1.0) in the 470–570 nm range for autofluorescence intensity and in the 380-410 nm range for SHG. The latter range corresponds to half the excitation wavelength, consistent with the theoretical SHG emission (26). Autofluorescence lifetime was measured in the 420-460 nm range, where reduced nicotinamide adenine dinucleotide (phosphate) [NAD(P)H] intrinsic fluorescence is predominantly expected (27,28). Intensity contrast images were acquired with 2.0% laser power (2.90 W), using a 450 V detector for autofluorescence and a 720 V detector for SHG. Laser power and detector settings were kept constant for both hyperoxia and normoxia samples. To ensure representative sampling and minimize scanning time, ten mosaics (2.7 mm^2 each) were randomly acquired from each lung section, taking approximately 1 hour per section. Each mosaic comprised sixteen 1024×1024-pixel images (scan speed: 10 µs/pixel), which were automatically stitched using the Olympus FV31S-SW FLUOVIEW software. No digital zoom was applied, and the signal-to-noise ratio was enhanced by averaging two frames. The x, y, and z coordinates of each mosaic were recorded to facilitate subsequent acquisition following staining or immunolabeling. For fluorescence lifetime measurements, a 6× digital zoom was applied, and a minimum of ten additional randomly distributed 512×512-pixel images (scan speed: 12 µs/pixel) were acquired using 0.4%–0.8% laser power (2.90 W) and a detector voltage of 850 V. FLIM data were collected until a minimum of 10^5 counts per pixel were obtained within the region of interest. Calibration of the ISS FLIMbox system was performed using the known mono-exponential lifetime decay of fluorescein at pH 11.0 (4.0 ns upon excitation at 780 nm, collection range: 572–642 nm). Calibration samples were prepared by diluting a 100 mmol/L fluorescein stock solution in EtOH (1:2000) with 0.1 M NaOH (pH 11.0) prior to each session.

FLIM data analysis

Fluorescence lifetime is the time interval between photon absorption by a fluorophore and the subsequent emission of fluorescence (29). It is intrinsic to the molecular structure, highly sensitive to

conformational and microenvironmental changes, and largely independent from concentration (30), thus offering high discriminative power between tissues. Together with the intensity modulation, changes in fluorescence lifetime can represent an intrinsic “fingerprint” of disease (31).

FLIM data were analyzed using the phasor approach (29,32). Briefly, the fluorescence lifetime decay of each image pixel was measured and transformed via Fourier analysis into a point with coordinates G and S in the phasor plot. Each pixel in the image corresponds to a point in the phasor plot, and conversely, each cluster in the phasor plot represents a set of image pixels. Mono-exponential decays generate points along the universal semicircle, while multi-exponential decays distribute points within the semicircle. The position of these points reflects the intensity-weighted average contributions from individual mono-exponential decays.

Specifically, for each image, a cluster of points in the phasor plot was obtained, with each point corresponding to the lifetime of an image pixel. The centroids of these clusters were then calculated for each image and averaged to obtain a mean centroid for each sample. Only the G coordinates of these centroids were considered, as the S coordinates remained largely unchanged. Phasor centroid analysis and overall FLIM data processing were performed using SimFCS v. 4.0 software (Laboratory for Fluorescence Dynamics, University of California, Irvine).

SHG data analysis

SHG signals are detected exclusively within an emission range corresponding to half the illumination wavelength. To validate SHG specificity, lung slices were excited at 720 nm, 780 nm, and 840 nm. Emission signals were collected in the 380–410 nm range to selectively isolate SHG signals and in the 470–680 nm range to capture autofluorescence signals. True SHG signals were defined as those present in the 380–410 nm range when excited at 780 nm but absent when excited at 720 nm or 840 nm, ensuring the exclusion of autofluorescence artifacts.

Label-free histomorphometry

From each label-free mosaic all lung features listed below were extracted and manually or semi-automatically analyzed with Image J Fiji (33). These features were then used solely for a 2D quantitative histological evaluation. A complete summary of all features, including acquisition methodology, image analysis procedures, associated pathological significance, and corresponding conventional parameters, is provided in **Supplementary Table 1**.

Tissue density (TD) (%) – Tissue area was assessed using the HUANG (34) threshold-based mask applied to the autofluorescence channel for tissue selection. Huang thresholding had previously been applied to stained tissue for quantitative lung morphology elsewhere (35). From the total autofluorescence area, the area of alveolar exudates (for details, see "Density of alveolar exudates" in Materials and Methods) was excluded to focus solely on tissue segments. Tissue areas were then normalized by the acquisition area using the following formula:

$$TD\ (\%) = \frac{(Autofluorescence\ area - area\ of\ alveolar\ exudates)}{Mosaic\ area} \times 100$$

Tissue autofluorescence intensity – Autofluorescence intensity was quantified in tissue segments. Tissue selection was performed using a HUANG (34) threshold-based mask applied to the autofluorescence channel. The average tissue intensity was then normalized to the background intensity using the following formula:

$$Tissue\ autofluorescence\ intensity\ = \frac{Tissue\ Autofluorescence\ intensity}{Background\ autofluorecence}$$

Density of alveolar exudates (%) – Alveolar exudates were measured using the autofluorescence channel. Exudates accumulated in the alveolar spaces were manually selected and the total area was calculated. The area was then normalized to the mosaic area using the following formula:

$$Density\ of\ alveolar\ exudates\ (\%) = \frac{Area\ alveolar\ exudates}{Mosaic\ area} \times 100$$

Density of parenchymal collagen (%) – Fibrillar collagen was assessed using the SHG channel. To eliminate background noise caused by the bleed-through of autofluorescence emitted by spot-like structures and red blood cells (RBCs), autofluorescence was subtracted. This process ensured that only pixels with a true SHG signal were retained for collagen evaluation. Quantification was performed by applying the "Frangi vesselness filter" (36) version "imglib, experimental", available on ImageJ Fiji. Originally developed as a vessel enhancement filter, the Frangi filter has also been applied to detect tube-like structures such as collagen fibers (37). Filter parameters were optimized by testing multiple combinations and comparing their detection capabilities in our images. The chosen parameters were: 'number of scales' = 1, 'minimum scale' = 0.9, 'maximum scale' = 5. To selectively identify collagen in the alveolar septa and interstitial spaces, four regions of interest (ROIs) of 0.237 mm² were selected within each mosaic to avoid airways, and muscularized vessels. The ROIs selection was exclusively performed on the autofluorescence channel to minimize the selection bias. Otsu's threshold was then applied to the SHG channel to select areas occupied by fibers. The collagen area was subsequently normalized by the ROI area using the following formula:

$$Parenchymal\ collagen\ (\%) = \frac{Area\ SHG\ collagen}{ROI\ area} \times 100$$

Alveolar density – A ROI of 0.866 mm² was selected at the same central position of each mosaic to manually count all enclosed surfaces, excluding airways, vessels, and alveolar sacs, while including individual alveoli, thus providing an approximation of the alveolar count **(Supplementary Figure 1)**. The excluded structures were recognized using their peculiar autofluorescence and SHG signal combination. The number of alveoli was then normalized by the ROI area and a multiplicative factor of 10^4 was applied, using the following formula:

$$Alveolar\ density = \frac{Count\ of\ enclosed\ surfaces\ *}{ROI\ area} \times 10^4$$

*No airways, vessels, alveolar sacs

Arterial medial thickness (MT) (%) and Arterial adventitia thickness (ADVT) (%) – MT% and ADVT% were evaluated by combining the SHG and autofluorescence channels. For MT% we adapted the method previously described in (13). For each animal, ten muscularized vessels with an external short-side diameter between 50 µm and 100 µm, identified in the mosaics and corresponding to pre-and intra-acinar arteries in rabbits, were selected. MT% was calculated by measuring the external short-side diameter excluding SHG signals (ED) and the internal short-side diameter (ID), which considered only the lumen **(Supplementary Figure 2)**, using the following formula (22):

$$MT\ (\%) = \frac{ED - ID}{ED} \times 100$$

ADVT% was determined on the same vessels by measuring the external short-side diameter including SHG signals (AED) and using the previously measured ED as the internal diameter, which encompasses both the lumen and internal layers **(Supplementary Figure 2)**, applying the following formula:

$$ADVT\ (\%) = \frac{AED - ED}{AED} \times 100$$

Principal Component Analysis (PCA)

PCA was performed on MATLAB, by means of the built-in function providing the principal components, explained variances, and scores. The results were analyzed to understand variance contributions, and scatterplots were generated for visualization. Confidential ellipsoids were calculated using the eigenvalues and eigenvectors of a covariance matrix in MATLAB. The eigenvalues define the axes' lengths, while the eigenvectors determine their orientation in space. This representation visualizes uncertainty in multivariate data by scaling the ellipsoid according to the confidence level.

Statistical analysis

Statistical analysis was performed using GraphPad Prism (GraphPad 8.0.1, San Diego, CA, USA). Normality tests were performed with Shapiro-Wilk, variance tests with test F and outliers' identifications with ROUTE method (Q = 1%). Information on the statistical test used is provided in the description of each figure and it is in accordance with data distribution. Correlation tests were performed using Person or Spearman tests depending on whether the variables were normally distributed or not. For linear regression analysis, regression coefficients and goodness of fit (R^2) were reported in figure description. Levels of significance used: ns = $p > 0,05$, * $p \leq 0,05$, ** $p \leq 0,01$, *** $p \leq 0,001$, **** $p \leq 0,0001$.

Results

Designing a multi-channel acquisition system for label-free simultaneous visualization of lung parenchymal structures

As detailed in materials and methods, lung sections were collected from rabbits delivered prematurely at 28 GA and exposed to hyperoxia (95% O_2, n=6) for 7 days to mimic severe BPD (**Figure 2a**). Animals cared under normoxia (21% O_2, n=6) were used as controls (**Figure 2a**). In the proposed approach for image acquisition, we employed a TPEF microscope. The laser was set to 780 nm, and a multi-channel detection system was designed to simultaneously capture tissue autofluorescence intensity, lifetime and SHG signals from collagen in the 470-570 nm, 420-460 nm and 380-410 nm ranges, respectively (**Figure 2b**). To acquire tissue autofluorescence intensity and SHG signals, we used an optimized protocol involving random acquisition of 10 mosaics (each covering 2.71 mm²), with 16 frames per mosaic for each section (**Figure 2c**). As illustrated in **Figure 2d**, the integration of autofluorescence intensity and SHG signals enabled the simultaneous label-free detection of lung parenchymal parameters relevant to BPD, including TD, autofluorescence intensity, alveolar exudates, fibrillar collagen deposition, arterial layers and alveolar density. Beyond these, autofluorescence lifetime provides an additional source of image contrast (for details and definition, see Materials and Methods). Lifetime measurements were performed on ten randomly selected

regions at higher magnification and summarized using a phasor centroid **(Figure 2e),** providing a distinctive signature that can help discriminate between normoxic and hyperoxic conditions.

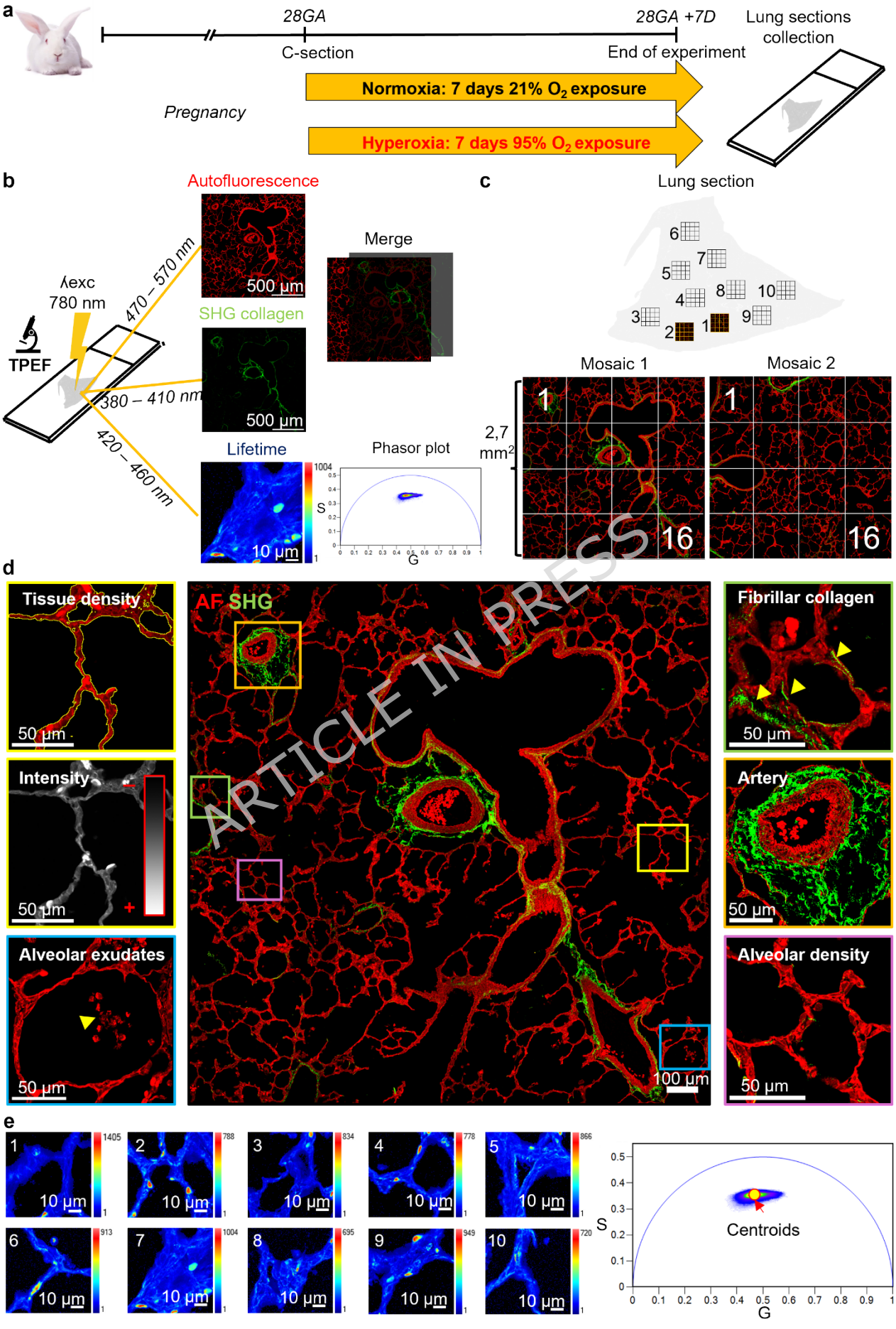

Figure 2. Multichannel imaging system enabling simultaneous visualization of lung parenchymal features in preterm rabbit tissue sections. (a) Lung sections (5 μm) were obtained from preterm rabbits extracted at 28 GA randomly assigned to normoxia (21% O_2, n=6) or hyperoxia (95% O_2, n=6) for seven days. Paraffin was removed from lung sections before label-free imaging**. (b)** TPEF of lung sections at 780 nm and simultaneous acquisition of autofluorescence intensity in the 470–570 nm range, SHG of collagen in the 380–410 nm range, and autofluorescence lifetime in the 420–460 nm range through an optimized multichannel acquisition system. **(c)** The optimized acquisition protocol for autofluorescence intensity and SHG which involved random acquisition of 10 mosaics (each 2.71 mm^2) per lung slice, with 16 frames per mosaic. **(d)** Representative image of all features that can be simultaneously analyzed in each mosaic using autofluorescence (red signal) and SHG imaging (green signal). These features include tissue density and intensity of its autofluorescence (yellow boxes), alveolar exudates (light blue box and indicated by arrowhead), fibrillar collagen (green box and indicated by arrowhead), arteries (orange box), and alveolar density (pink box). **(e)** Ten additional randomly distributed regions within the same lung sections were selected for autofluorescence lifetime measurement. Representative FLIM images of the ten regions depicted the distribution of fluorescence intensity (left) with each pixel having a corresponding point in their phasor plot (right). The resulting cluster centroid represented the sample's lifetime signature. Images of SHG signal were presented after autofluorescence subtraction.

Autofluorescence-based features: hyperoxia exposure induces increased tissue density, inflammation and reduced autofluorescence intensity

Lung parenchymal development and inflammation are traditionally assessed using H&E-stained sections (6,11,13), which effectively highlight tissue morphology and cellular components. Autofluorescence imaging in the 470–570 nm range revealed lung morphology comparable to that observed in H&E-stained sections (**Figure 3a**). Additionally, autofluorescence effectively visualized cells of the airways epithelium, blood vessels, and alveolar exudates (**Supplementary Figure 3**). Compared to normoxic controls, hyperoxia-exposed lungs displayed septal thickening and elevated alveolar exudates (**Figure 3b**). To confirm these observations, we developed an autofluorescence-based method for quantifying TD and alveolar exudates. Among the tested thresholding approach (e.g., Otsu (38), Percentile), the Huang method (34) provided the most accurate tissue segmentation and was therefore used for TD analysis **(Supplementary Figure 4)**.

During inflammation, alveolar spaces become filled with immune-cell infiltrates, primarily neutrophils with fewer macrophages, as well as proteinaceous debris, including fibrin strands and hyaline membranes (23). Alveolar exudates emit autofluorescence (**Supplementary Figure 5**) and were more prominent in the lung sections of rabbit pups exposed to hyperoxia (**Figure 3b**), as corroborated by H&E-stained slices (**Supplementary Figure 6**). Since thresholding methods indiscriminately select all autofluorescent elements, alveolar exudates were initially included in TD calculations (**Supplementary figure 7**). To address this, we quantified the exudates separately as an indicator of inflammation and subtracted their area from the total tissue measurement (for details, see Materials and Methods). Hyperoxia exposure resulted in a significant increase in TD% (**Figure 3c**), attributed to septal thickening, as corroborated by H&E staining on the same tissue sections (**Supplementary Figure 6**). Additionally, a clear trend toward increased alveolar exudates % was observed in hyperoxic samples (**Figure 3d**).

Notably, alveolar exudates showed a patchy distribution across lung sections and exhibited substantial variability in overall quantity within the hyperoxia group (**Supplementary Figure 8**).

In addition, we measured autofluorescence intensity using the Huang thresholding approach (34). Autofluorescence signal intensity depends on the composition and intrinsic fluorescence properties of endogenous molecules that are excited and emit within the spectral range considered. Therefore, variations in autofluorescence intensity may serve as intrinsic indicators of compositional changes characteristic of disease states (31), which in this case is related to oxygen injuries. Under identical acquisition settings, hyperoxic lung tissue exhibited ~2 units lower autofluorescence intensity compared to normoxic tissue (**Supplementary Figure 9**). While the biological basis of this difference was not explored in detail, we identified highly autofluorescent, spot-like structures in both normoxic and hyperoxic lungs that may have influenced overall signal intensity. These structures exhibited spectral and lifetime characteristics consistent with RBCs (**Supplementary Figures 10**), suggesting that they may represent RBCs trapped within capillaries.

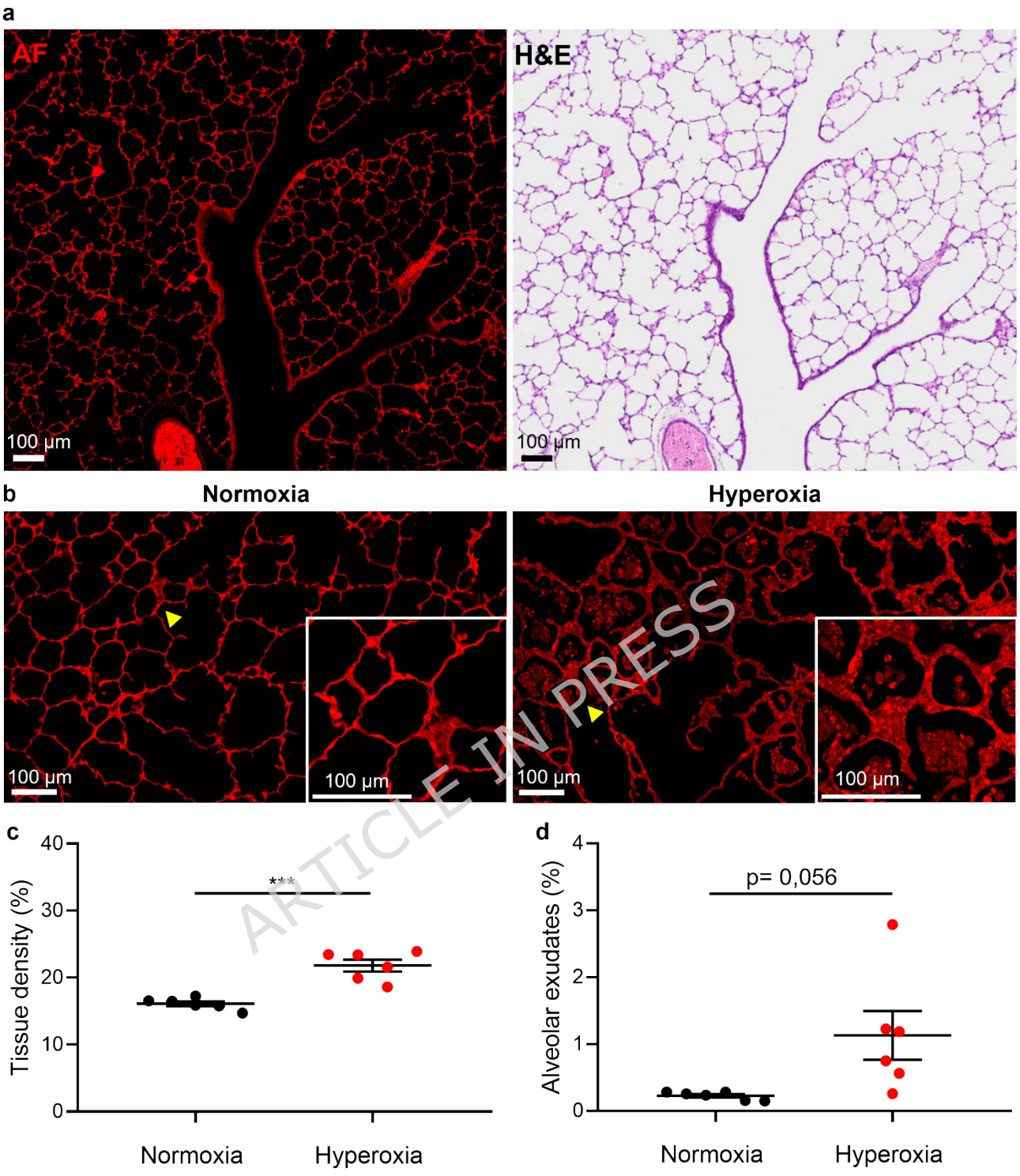

Figure 3. Autofluorescence-based features: TD and alveolar exudates. (a) Autofluorescence imaging reveals lung morphology comparable to that observed in the corresponding H&E-stained section. Representative comparison between (left) tissue autofluorescence and (right) the H&E staining of the same histological section. **(b)** Representative images of tissue autofluorescence signal from Normoxia (left) and Hyperoxia (right) preterm rabbits showing hyperoxia-induced septal thickening and increased alveolar exudates. Yellow arrowheads indicate the magnified regions. **(c)** Scatter plot of the percentage of tissue density calculated from tissue autofluorescence signal using a Huang-based thresholding mask,

and by subtracting the area of alveolar exudates from the tissue area, in lung sections from n = 6 normoxia and n = 6 hyperoxia preterm rabbits. Statistical difference was assessed using unpaired t test and Mean ± SEM were presented for both conditions. **(d)** Scatter plot of the percentage of alveolar exudates measured on tissue autofluorescence in lung sections from n = 6 normoxia and n = 6 hyperoxia preterm rabbits. The statistical difference was assessed using Welch t test (populations had different variances) and Mean ± SEM were represented for both conditions.

SHG-based feature: hyperoxia exposure induces increased fibrillar collagen deposition

To assess collagen fiber deposition following hyperoxia exposure, we incorporated a dedicated channel for acquiring SHG signals. SHG is widely used for collagen quantification due to its non-centrosymmetric structure (39). This phenomenon occurs when two incident waves interact with a non-centrosymmetric material, generating an output wave with half the wavelength of the incident waves (26). In our study, lung sections were excited at 780 nm, and a 380–410 nm bandpass filter was applied to isolate SHG signals while minimizing background autofluorescence. To confirm the specificity of SHG for collagen, a subset of the same tissue sections was stained with PSR, a widely used histological/fluorescent marker for fibrillar collagen (6,24,25,40). We noted a consistent qualitative association between the SHG signal and PSR fluorescence (**Figure 4a**). Prior to collagen analysis, image processing was performed to remove background noise. Specifically, autofluorescence was subtracted to eliminate interference from highly autofluorescent structures such as RBCs and other spot-like features (**Supplementary Figure 11**). These structures were verified not to emit true SHG signals, as their emissions remained present in the 380–410 nm range when excited at 720 nm and 840 nm (**Supplementary Figure 12**), confirming that they were not fibrillar collagen components.

SHG-based comparisons revealed an increase in collagen deposition in hyperoxia-exposed lung parenchyma, suggesting mild fibrosis (**Figure 4b**). In normoxia conditions, collagen appeared to be primarily localized at secondary septal tips (yellow arrowheads in **Figure 4b**), consistent with areas of active alveolarization (**Supplementary Figure 13**). The higher collagen deposition in hyperoxia-exposed animals was further qualitatively verified by immunohistochemistry with a Col1a1 antibody,

which specifically detects collagen I, and by PSR staining on normoxia and hyperoxia consecutive tissue sections (**Supplementary Figure 14**).

To quantitatively assess parenchymal collagen deposition, we applied the Frangi Vesselness filter (36), which, in combination with Otsu thresholding, provided the most reliable detection of collagen fiber among the tested filters (e.g., CLAHE (41), Median Filter (42)) **(Supplementary Figure 15)** (for details, see Materials and Methods). Quantitative analysis confirmed the qualitative findings, revealing a significant 2.6-fold increase in parenchymal collagen deposition in hyperoxia-exposed tissues (**Figure 4c**).

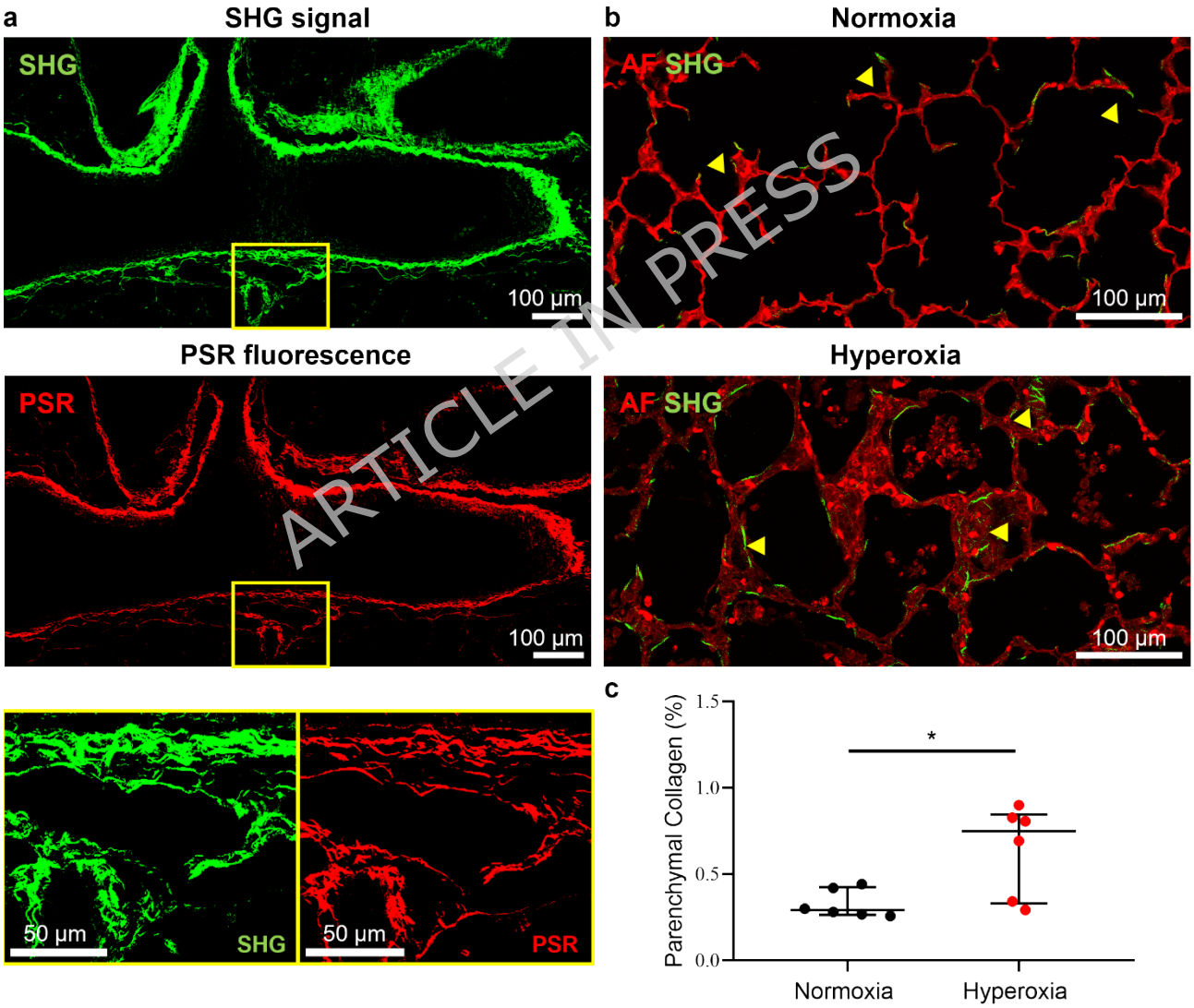

Figure 4. SHG-based features: Fibrillar collagen content. (a) Representative images comparing the SHG signal (top) and PSR fluorescence (bottom) on the same lung section. Whenever an SHG signal was detected, a corresponding PSR signal was also observed (yellow boxes). **(b)** Representative images of the combination of SHG (green) and

autofluorescence (red) in lung sections from normoxia (top) and hyperoxia (bottom), showing increased collagen content in hyperoxia. In normoxia, collagen was primarily localized at the tips (yellow arrowheads), while in hyperoxia, abundant collagen deposition was observed in the alveolar septa and interstitial space (yellow arrowheads). **(c)** Scatter plot of the percentage of area occupied by parenchymal collagen fiber normalized by the area of acquisition, measured on lung sections from n=6 Normoxia and n=6 Hyperoxia preterm rabbits. To specifically measure parenchymal collagen, regions without muscularized vessels and airways were selected from the autofluorescence channel. Mann-Whitney test; Median ± interquartile range (IQR) are presented for both conditions. Notably, images and analysis of SHG signal were presented after autofluorescence subtraction as detailed in materials and methods.

Autofluorescence and SHG-based features: hyperoxia exposure induces increased MT%, and reduced alveolar density

By combining autofluorescence and SHG acquisitions, we assessed two additional features: arterial wall thickness and alveolar density. Arteries were readily identifiable in label-free images (**Figure 5a**). The outer layer exhibited strong SHG signals, which may correspond to the collagen-rich *tunica adventitia*, while the inner layers showed autofluorescence from cells and elastin, characteristic of the *tunica media* and *intima* (**Figure 5a**). RBCs were sometimes present within the lumen (**Figure 5a**). In the tunica media, layers of spindle cell characterized by autofluorescent cytoplasm and dark, elongated nuclei were distinguishable (**Figure 5a**). Smooth muscle cells were identified by immunostaining with an anti- α-SMA antibody (**Figure 5b**). Endothelial cells were occasionally identifiable within the *tunica intima* (**Figure 5a**), as confirmed by anti- CD31/PECAM-1 staining (**Supplementary Figure 16**).

As a surrogate of arterial remodeling, we measured the MT%, a well-established indicator of vascular impairment in BPD (11,13,17), together with ADVT% (for details, see Materials and Methods). Hyperoxia-exposed tissues showed arterial wall thickening **(Figure 5c)** with a significant 2.4-fold increase of MT% (**Figure 5d**), while ADVT% remained unchanged **(Supplementary Figure 17)**.

Furthermore, using an alveolar density metric derived from autofluorescence and SHG signals as a surrogate of alveolarization (for details, see Materials and Methods), we found an approximate 22%

reduction in alveolar density in hyperoxia-exposed lungs, indicative of alveolar simplification. **(Figure 5e)**.

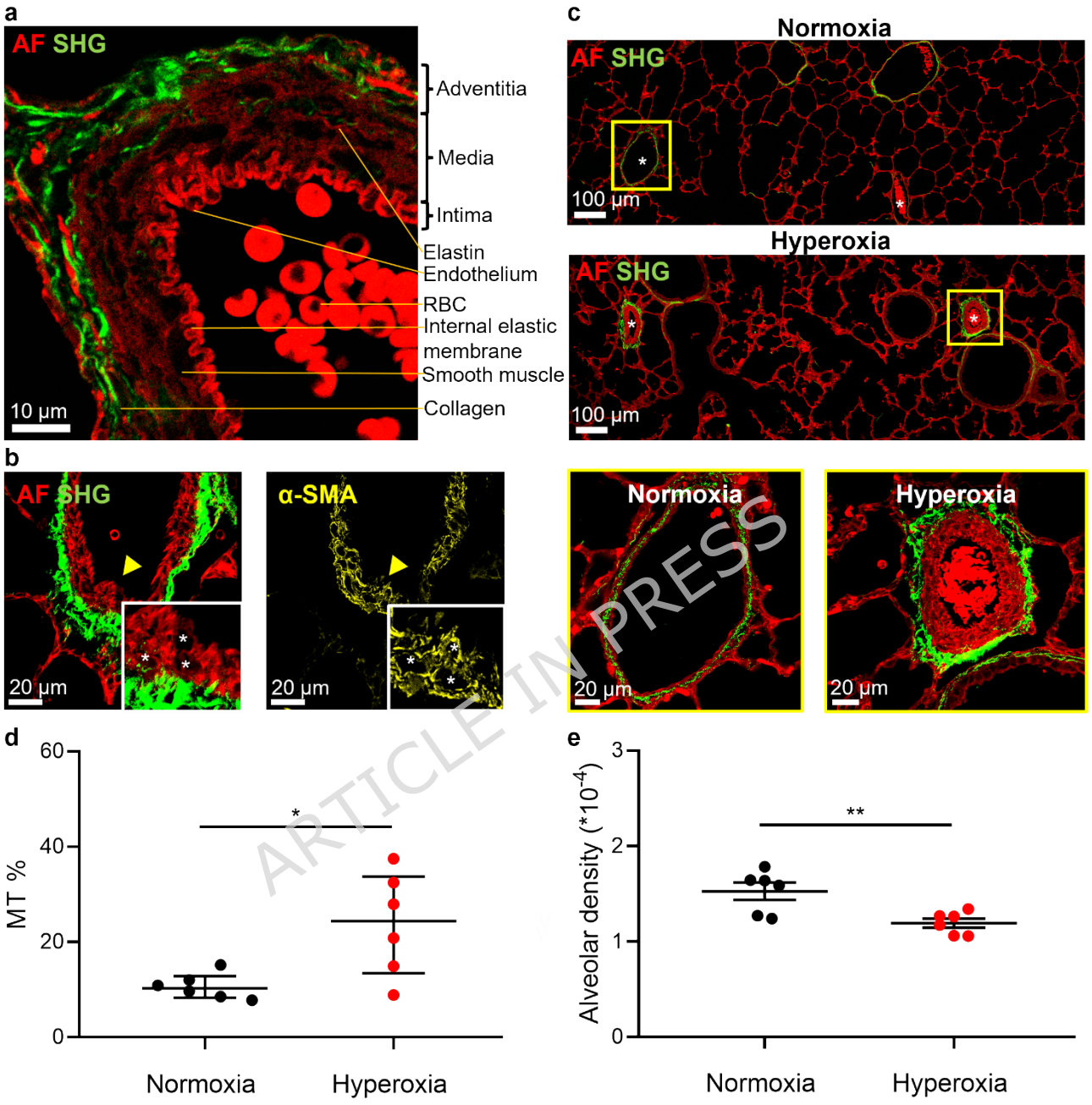

Figure 5. Autofluorescence and SHG-based features: MT% and alveolar density. (a) Representative image of the label-free appearance of arteries by combining autofluorescence (in red) and SHG (in green). Each line corresponds to a different component listed in the figure. **(b)** Smooth muscle layer of *tunica media* was identified label-free (left) and smooth muscle cell confirmed by using anti- α-SMA antibody on the same lung slice (right). The yellow arrowheads indicate magnified regions. **(c)** Representative comparison between normoxia (top) and hyperoxia (bottom) showing arterial wall thickening in hyperoxia. AF in red, and SHG, in green. Asterisks indicate arteries with ED between 50 and

100 µm. Yellow boxes indicate magnified regions. **(d)** The scatter plot shows the MT% measured on lung sections from n=6 Normoxia and n=6 Hyperoxia preterm rabbits. Mann-Whitney test; Median ± IQR are presented. **(e)** Scatter plot of alveolar density measured on lung sections from n=6 normoxia and n=6 hyperoxia preterm rabbits (Unpaired *t*-test; mean ± SEM are presented). The count of airspaces was normalized to the ROI area and scaled by a constant factor of 10^4. Notably, images of SHG signal were presented after autofluorescence subtraction as detailed in materials and methods.

Autofluorescence lifetime-based feature: hyperoxia exposure induces shift toward longer tissue autofluorescence lifetime

A further analysis was conducted using FLIM to identify tissue autofluorescence lifetime of lung sections under normoxia and hyperoxia conditions. Fluorescence lifetime, like intensity signal, is a property of fluorescence that depends on the composition of endogenous fluorophores within the tissue. Unlike intensity, autofluorescence lifetime is more sensitive to tissue molecular composition, as it is independent of fluorophore concentration and reflects the local microenvironment (43). Consequently, tissue autofluorescence lifetime provides an additional layer of contrast to distinguish between hyperoxic and normoxic tissues. The measured lifetimes, upon phasor transformation (for details, see Materials and Methods), showed an elongated distribution within the universal semi-circle in both conditions with phasor centroids shifted toward longer lifetime in hyperoxia (**Figure 6a**). This observation was confirmed by measuring the G coordinate of centroids in both conditions (**Figure 6b**). This shift reflects intrinsic molecular differences which could be leveraged for automated tissue recognition without prior knowledge and warrants further investigation into its underlying causes.

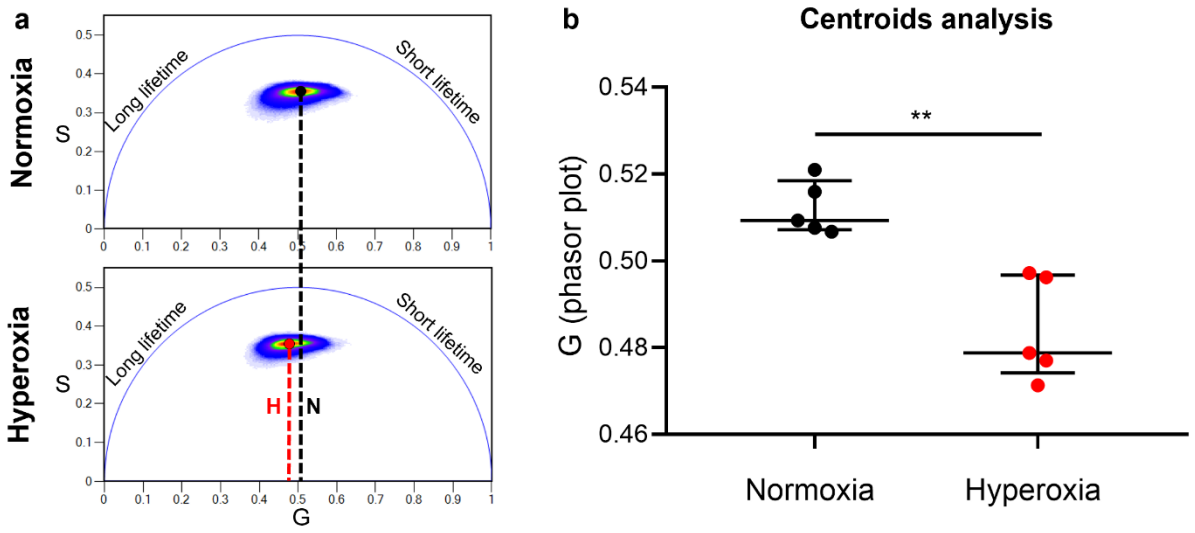

Figure 6. Hyperoxia-induces a shift toward longer tissue autofluorescence lifetime. (a) Phasor plots describing the autofluorescence lifetime of normoxia (top) or hyperoxia (bottom) lung sections. Shifting of autofluorescence lifetime can be modeled using phasor centroids (dark dot normoxia "N" and red dot hyperoxia "H") and its movement between the two conditions. **(b)** Quantitative measurements of centroids shift along G axis. Scatter plot of the G coordinates of the centroids measured for each cluster of points in the phasor plot for each of the n = 5 normoxia rabbits and n = 5 hyperoxia rabbits**.** Statistical difference was assessed using the Mann-Whitney test, with the median ± IQR presented for both conditions (Δ median = 0.031). The S coordinate was not considered because it did not differ significantly.

Label-free histomorphology correlates with H&E findings and lung function

To further validate our findings, we performed correlation analyses between label-free parameters for alveolar and vascular assessments, specifically alveolar density, alveolar exudates, and MT%, and conventional measurements obtained from H&E-stained sections of the same animals, including RAC, ALI score, and MT%, respectively. Notably, all three label-free parameters showed strong correlations with the conventional BPD-related histomorphometric measurements (**Figure 7a–c**). Specifically, alveolar density correlated with RAC (r = 0.85) (**Figure 7a**); alveolar exudates correlated with the ALI score (23) (r = 0.82) (**Figure 7b**); and MT% values derived from label-free imaging correlated with those obtained from H&E-stained sections (r = 0.87) (**Figure 7c**). These results further demonstrate the robustness of the method and the reliability of our analysis in detecting hyperoxia-induced alterations.

Before collecting lung sections, functional parameters (IC/bw, G, H, Cst/bw) were measured in live animals using the FlexiVent device **(Supplementary Figure 18)**. The goal was to test whether the severity of histological alterations detected by the label-free approach reflected the degree of lung function impairment in the same animals, thus further supporting the reliability of the method. Two PCAs were performed, one for label-free histology and one for lung function, using the measured parameters **(Supplementary Figure 19 a-b)**. The first principal component (PC1) from each, accounting for most data variance and to which all features from the respective analyses contributed, with TD% and AF lifetime showing the largest contribution in histological PC1 and Cst/bw and IC/bw in the functional PC1 **(Supplementary figure 19 a-b)**, was used as an overall *Histological* and *Functional Score* (higher PC1 = greater severity). The two scores showed a strong positive correlation ($r = 0.85$, $p = 0.0004$), with normoxia and hyperoxia groups clearly separated at opposite ends of a shared linear trend ($R^2 = 0.72$) **(Figure 7d)**. This result confirmed that functional impairments were consistently associated with histological alterations detected by the label-free method. Pairwise correlations between individual parameters are shown in **Supplementary Figure 20**.

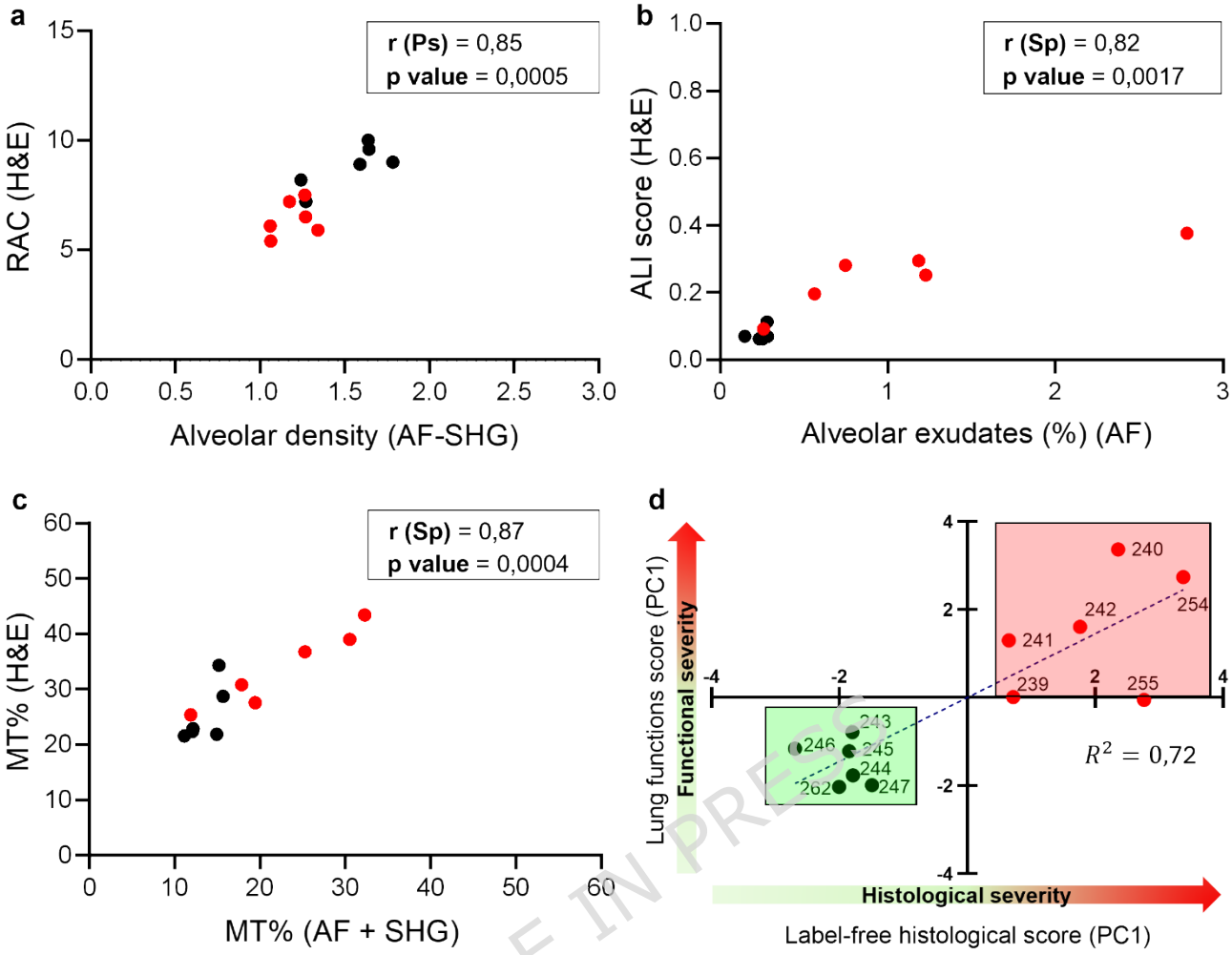

Figure 7 Label-free histomorphological features correlate with H&E-based findings and lung function metrics. Black dots were normoxia rabbits (n=6), while red dots were hyperoxia rabbits (n=6). **(a)** Pearson correlation test between alveolar density measured from label-free signals and RAC calculated in H&E-stained lung sections from the same rabbits. **(b)** Spearman correlation test between the percentage of alveolar exudates measured on the autofluorescence signal, and the ALI score measured in H&E-stained lung sections from the same rabbits. **(c)** Spearman correlation test between the MT% measured on label-free signals and those calculated in H&E-stained lung sections from the same rabbits. **(d)** Correlation between the overall histological and functional profiles of preterm rabbits. The "label-free Histological Score (PC1)" (X-axis) and "Lung Functional Score (PC1)" (Y-axis) were derived from the first principal component (with sign-inverted) of the respective PCAs. PC1 was selected because it accounts for most of the data variability in the analyses. Pearson's r = 0.85, p = 0.0004. Linear regression: $Y = 0.7245X - 7.735e^{-8}$, $R^2 = 0.72$.

Discussion

In this study, we present a label-free, multi-channel imaging approach that enables qualitative and quantitative assessment of lung parenchymal alterations in a preterm rabbit model of BPD. By

integrating TPEF, SHG, and FLIM, we successfully visualized key pathological hallmarks of hyperoxia-induced lung injury, including increased TD, alveolar exudates, collagen deposition, vascular alterations, and alveolar simplification. The presented method provides a reliable approach that supports conventional histology and immunolabeling for lung tissue characterization in preclinical BPD research.

The preterm rabbit exposed to hyperoxia has recently been proposed for pharmacological studies on BPD (9). The preterm rabbit combines the easy handling and large litter size of small animals with the ability to mimic prematurity (10) and human-like lung development (6). Furthermore, exposing preterm rabbit (28GA) to 95% oxygen for seven days has been shown to effectively reproduce histopathological features of human BPD, including impaired alveolar and vascular development, inflammation, and ECM remodeling (9). However, working with rabbits also presents certain limitations, such as the limited availability of validated antibodies (9), which restricts the analyses primarily to functional and histological outcomes. Histological assessment may require multiple staining to study key relevant BPD features. Here we present a non-destructive, label-free method for in-depth analysis of pulmonary architecture in lung slices from premature rabbits. By exploiting tissue intrinsic autofluorescence, our approach effectively identified increased TD, associated with septal thickening, as well as increased alveolar exudates in hyperoxia-exposed lungs. These findings are consistent with observations from serial sections stained with H&E, as well as with previous reports of hyperoxic lung injury in preterm rabbit models (6,11,17). The correlation between autofluorescence-based quantification of alveolar exudates and the ALI score from histological assessments of H&E-stained sections from the same animal further highlights the potential of this method, even if the evaluation of alveolar exudates is only one of the five parameters included in the ALI score. Inflammatory exudates exhibited distinct label-free signatures that could eventually be used to identify their composition. Given that “alveolar and interstitial edema” and “neutrophil infiltration into the alveolar space” are key components of the ALI score, we hypothesize that the

exudates observed predominately in the hyperoxic lungs may consist of a mixture of neutrophils and cell debris. Nevertheless, since we did not confirm the presence of neutrophils with immunostaining, we focused only on the total area to assess the magnitude of alveolar exudates as surrogate of the inflammatory response. Further investigations are required to explore the composition of the exudates in more detail.

The tissue autofluorescence intensity was also modulated, decreasing in tissues exposed to high oxygen levels. This change represents an intrinsic difference reflecting a structural or molecular adaptation to oxygen exposure. The underlying cause of this alteration requires further investigation.

Fibrillar collagens, especially types I and III, are key components of the lung interstitial matrix, ensuring structural integrity and regulating tissue stiffness (44). Dysregulated collagen deposition is a hallmark of both clinical and experimental BPD (45). Although less prominent in the "new" BPD, variable alveolar fibrosis persists in infant biopsies and autopsies (46,47), and increased collagen has been confirmed in BPD animal models (6,10,48–50). SHG-based analysis revealed enhanced fibrillar collagen deposition in the parenchyma of hyperoxic lungs, indicative of ECM remodeling and fibrosis, consistent with previous finding in preterm rabbit exposed to hyperoxia (6,10,17). These findings were qualitatively corroborated by PSR staining and immunolabeling for Col1a1, underscoring the robustness of our approach.

During lung development, pulmonary vascular and alveolar growth are tightly coordinated (51,52). In BPD, this coordination is disrupted, resulting in alveolar simplification and marked vascular and microvascular impairment that compromise gas exchange (47,53,54). Additionally, impaired angiogenesis and aberrant vascular remodeling, primarily characterized by increased arterial muscularization and tone (55), elevate the risk of pulmonary arterial hypertension (PH), a major contributor to morbidity and mortality in infants with BPD (3). Combining autofluorescence and SHG signals, our tool revealed a significant increase in MT% in hyperoxia-exposed lungs, closely matching values obtained from histological sections and consistent with previous studies (11,12,17).

Furthermore, alveolar density was significantly reduced in hyperoxia-exposed lungs, consistent with impaired alveolarization previously highlighted (11,12). Although RAC and alveolar density were based on different parenchymal features, both are related to the degree of alveolarization. The strong correlation between the label-free alveolar density metric and the RAC from H&E-stained sections further supports the validity of this technique for assessing lung developmental alterations.

FLIM provided an additional contrast layers, revealing a shift toward longer autofluorescence lifetimes in hyperoxic lungs. This change represents a sensitive and intrinsic signature of hyperoxia's effects, which could be used to distinguish between hyperoxic and normoxic lungs, especially in case of automated analysis, and warranting further investigation about its biological meaning.

By using all the optimized label-free features, the tool successfully discriminated between normoxic and hyperoxic preterm rabbits, highlighting the varying histological severity in hyperoxic rabbits. Furthermore, a strong correlation between the histological severity and the degree of lung function impairment assessed through Flexivent measurements was found.

The key rationale for employing this approach lies in its multiplexing capability and high information content. In contrast to conventional assessments, which often require multiple staining protocols on serial sections to characterize distinct pathological features, our platform enables the simultaneous visualization of alveolar, vascular, and ECM components from a single unstained slide, while remaining compatible with subsequent immunofluorescence or other staining procedures. Taken together, the approach allows integration and co-registration of multiple structural features, facilitating automated and quantitative analysis.

Eventually, these advantages can be implemented for drug screening, live tissue imaging and 3D applications. While the current study focuses on rabbit lung, the platform is broadly applicable to other tissues (e.g., rodent or human-derived samples), as it exploits intrinsic signals from conserved molecules (e.g., NAD(P)H, FAD, collagen, and elastin) (31).

Regarding practical considerations, the platform relies on standardized commercial multiphoton systems and open-source analytical tools, making the method implementable and replicable. Although it currently requires costly instrumentation and trained personnel, this aspect should be considered in light of its high-throughput screening potential which stems from both the multimodal acquisition system and the quantitative approach. The latter was designed to extract multiple parameters by leveraging primarily intrinsic signal contrasts, rather than direct, pathologist-based recognition, while still ensuring validation against expert pathological assessments. Therefore, its design is inherently suited for automation, and with improvements in acquisition through an autofocus system and workflow integration, this approach can evolve into a powerful, high-throughput imaging tool for routine preclinical research.

Nevertheless, this approach has certain limitations. While it provides valuable quantitative and high-resolution information on tissue structure, it does not offer molecular specificity attainable through immunolabeling. However, it can serve as an integrative platform that co-registers multiple features, creating an “optical fingerprint” to guide targeted molecular analyses. Combined with subsequent immunofluorescence, this co-registration can also generate annotated datasets suitable for training AI algorithms for label-free cell-type recognition (56).

Furthermore, the sampling strategy has limitations, as it does not cover the entire section and does not implement a fully unbiased stereological design, preventing the use of our approach for accurate volumetric estimation. However, our method follows well-established histological protocols and incorporates multiple measures, including standardized sample collection, random mosaic selection, and blind analysis, to ensure reproducibility and minimize bias, allowing robust 2D quantitative comparisons between groups.

Additionally, autofluorescence-based assessments may be influenced by the presence of highly fluorescent cellular components, such as RBCs, which require careful signal processing to exclude potential artifacts. Future studies should explore the integration of hyperspectral imaging, or

complementary molecular probes to enhance specificity. A more extensive use of lifetime measurements could also aid in this direction, as its application has been reported for collagen type identification (57), oxidative stress imaging (58) and inflammation composition (59).

Conclusion

This study introduces a novel imaging platform for both qualitative and quantitative assessment of hyperoxia-induced lung alterations in a preterm rabbit model of BPD. Our findings suggest that this label-free, non-destructive screening method can effectively capture key pathophysiological changes associated with hyperoxic exposure. With automated analysis, the approach holds promise as a powerful tool for preclinical research, enabling simultaneous evaluation of multiple pathological features in a single acquisition. Being compatible with standard histology and immunolabelling, this tool is envisioned to be integrated into preclinical workflows to complement and guide subsequent molecular analysis, thus providing a more comprehensive and efficient assessment of lung parenchyma alterations.

Abbreviations

BPD: Bronchopulmonary dysplasia

TPEF: Two-photon excitation fluorescence

SHG: Second harmonic generation

FLIM: Fluorescence lifetime imaging microscopy

GA: Gestational age

ECM: Extracellular matrix

RAC: Radial alveolar count

H&E: Hematoxylin and eosin

PSR: Picrosirius red

TD: Tissue density

C-section: Caesarian section

PND: Postnatal day

i.m.: Intramuscular

$\mathbf{V_T}$: Tidal volume

BR: Breath rate

PEEP: Positive end-expiratory pressure

IC: Inspiratory capacity

G: Tissue damping

H: Tissue elasticity

Cst: Static compliance

MT%: Medial thickness of arteries

ALI score: Acute lung injury score

ED: External diameter

ID: Internal diameter

HRP: Horseradish peroxidase

DAB: 3,3'-diaminobenzidine

Col1a1: Collagen type I alpha 1 chain

α-SMA: Alfa smooth muscle actin

TRIS-HCL: Tris(hydroxymethyl)aminomethane hydrochloride

EDTA: Ethylenediaminetetraacetic acid

SDS: Sodium dodecyl sulfate

RT: Room temperature

PBST: TritonX-100 in PBS

ON: Overnight

CD31/PECAM-1: Cluster of differentiation 31

BSA: Bovine serum albumin

DAPI: 4',6-diamidino-2-phenylindole

NAD(P)H: Reduce nicotinamide adenine dinucleotide (phosphate)

RBCs: Red blood cells

ADVT%: Adventitial thickness of arteries

AED: External diameter including SHG

PCA: Principal component analysis

PH: Pulmonary hypertension

References

1. Thébaud B, Goss KN, Laughon M, Whitsett JA, Abman SH, Steinhorn RH, et al. Bronchopulmonary dysplasia. Vol. 5, Nature Reviews Disease Primers. Nature Publishing Group; 2019.

2. Jobe AH, Bancalari E. NICHD / NHLBI / ORD Workshop Summary. Am J Respir Crit Care Med. 2001;163.

3. Schmidt AR, Ramamoorthy C. Bronchopulmonary dysplasia. Vol. 32, Paediatric Anaesthesia. John Wiley and Sons Inc; 2022. p. 174–80.

4. Hilgendorff A, O'Reilly MA. Bronchopulmonary dysplasia early changes leading to long-term consequences. Vol. 2, Frontiers in Medicine. 2015.

5. Baraldi E, Carraro S, Filippone M. Bronchopulmonary dysplasia: Definitions and long-term respiratory outcome. Early Hum Dev. 2009;85.

6. Richter J, Toelen J, Vanoirbeek J, Kakigano A, DeKoninck P, Verbeken E, et al. Functional assessment of hyperoxia-induced lung injury after preterm birth in the rabbit. Am J Physiol Lung Cell Mol Physiol. 2014;306(3).

7. O'Reilly M, Thébaud B. Animal models of bronchopulmonary dysplasia. The term rat models. Vol. 307, American Journal of Physiology - Lung Cellular and Molecular Physiology. 2014.

8. Berger J, Bhandari V. Animal models of bronchopulmonary dysplasia. The term mouse models. Vol. 307, American Journal of Physiology - Lung Cellular and Molecular Physiology. 2014.

9. Salaets T, Gie A, Tack B, Deprest J, Toelen J. Modelling bronchopulmonary dysplasia in animals: arguments for the preterm rabbit model. Curr Pharm Des. 2017.

10. Manzano RM, Mascaretti RS, Carrer V, Haddad LB, Fernandes AR, Reyes AMA, et al. A hyperoxic lung injury model in premature rabbits: The influence of different gestational ages and oxygen concentrations. PLoS One. 2014;9(4).

11. Jiménez J, Richter J, Nagatomo T, Salaets T, Quarck R, Wagennar A, et al. Progressive vascular functional and structural damage in a bronchopulmonary dysplasia model in preterm rabbits exposed to hyperoxia. Int J Mol Sci. 2016;17(10).

12. Mühlfeld C, Schulte H, Jansing JC, Casiraghi C, Ricci F, Catozzi C, et al. Design-Based Stereology of the Lung in the Hyperoxic Preterm Rabbit Model of Bronchopulmonary Dysplasia. Oxid Med Cell Longev. 2021;2021.

13. Storti M, Faietti ML, Murgia X, Catozzi C, Minato I, Tatoni D, et al. Time-resolved transcriptomic profiling of the developing rabbit's lungs: impact of premature birth and implications for modelling bronchopulmonary dysplasia. Respir Res. 2023;24(1).

14. Catozzi C, Stretti F, Scalera E, Storti M, Modena A, Aquila G, et al. Single, double, and triple-hit strategies to establish a long-term premature rabbit model of bronchopulmonary dysplasia. Respir Res. 2025 Dec 1;26(1):35.

15. Suvarna SK, Layton C, Bancroft JD. Bancroft's Theory and Practice of Histological Techniques, Eighth Edition. Bancroft's Theory and Practice of Histological Techniques, Eighth Edition. 2018.

16. Tadrous PJ. Diagnostic Criteria Handbook in Histopathology: A Surgical Pathology Vade Mecum. Diagnostic Criteria Handbook in Histopathology: A Surgical Pathology Vade Mecum. 2008.

17. Salaets T, Tack B, Jimenez J, Gie A, Lesage F, de Winter D, et al. Simvastatin attenuates lung functional and vascular effects of hyperoxia in preterm rabbits. Pediatr Res. 2020;87(7).

18. Salaets T, Gie A, Jimenez J, Aertgeerts M, Gheysens O, Velde G Vande, et al. Local pulmonary drug delivery in the preterm rabbit: Feasibility and efficacy of daily intratracheal injections. Am J Physiol Lung Cell Mol Physiol. 2019;316(4).

19. Aquila G, Regin Y, Murgia X, Salomone F, Casiraghi C, Catozzi C, et al. Daily Intraperitoneal Administration of Rosiglitazone Does Not Improve Lung Function or Alveolarization in Preterm Rabbits Exposed to Hyperoxia. Pharmaceutics. 2022;14(7).

20. Thurlbeck WM. The radial alveolar count method of Emery and Mithal: A reappraisal 2-Intrauterine and early postnatal lung growth THOMAS P Cooney. Thorax. 1982;37(8).

21. Emery JL, Mithal A. The number of alveoli in the terminal respiratory unit of man during late intrauterine life and childhood. Arch Dis Child. 1960;35(184).

22. Roubliova XI, Deprest JA, Biard JM, Ophalvens L, Gallot D, Jani JC, et al. Morphologic changes and methodological issues in the rabbit experimental model for diaphragmatic hernia. Histol Histopathol. 2010;25(9).

23. Matute-Bello G, Downey G, Moore BB, Groshong SD, Matthay MA, Slutsky AS, et al. An official american thoracic society workshop report: Features and measurements of experimental acute lung injury in animals. In: American Journal of Respiratory Cell and Molecular Biology. 2011. p. 725–38.

24. Dolber PC, Spach MS. Conventional and confocal fluorescence microscopy of collagen fibers in the heart. Journal of Histochemistry and Cytochemistry. 1993;41(3).

25. Wegner KA, Keikhosravi A, Eliceiri KW, Vezina CM. Fluorescence of Picrosirius Red Multiplexed With Immunohistochemistry for the Quantitative Assessment of Collagen in Tissue Sections. Journal of Histochemistry and Cytochemistry. 2017;65(8).

26. Mostaço-Guidolin L, Rosin NL, Hackett TL. Imaging collagen in scar tissue: Developments in second harmonic generation microscopy for biomedical applications. Vol. 18, International Journal of Molecular Sciences. 2017.

27. Chance B, Schoener B, Oshino R, Itshak F, Nakase Y. Oxidation-reduction ratio studies of mitochondria in freeze-trapped samples. NADH and flavoprotein fluorescence signals. Journal of Biological Chemistry. 1979;254(11).

28. Azzarello F, Pesce L, De Lorenzi V, Ferri G, Tesi M, Del Guerra S, et al. Single-cell imaging of α and β cell metabolic response to glucose in living human Langerhans islets. Commun Biol. 2022;5(1).

29. Stringari C, Cinquin A, Cinquin O, Digman MA, Donovan PJ, Gratton E. Phasor approach to fluorescence lifetime microscopy distinguishes different metabolic states of germ cells in a live tissue. Proc Natl Acad Sci U S A. 2011;108(33).

30. Datta R, Heaster TM, Sharick JT, Gillette AA, Skala MC. Fluorescence lifetime imaging microscopy: fundamentals and advances in instrumentation, analysis, and applications. J Biomed Opt. 2020;25(07).

31. Zipfel WR, Williams RM, Christie R, Nikitin AY, Hyman BT, Webb WW. Live tissue intrinsic emission microscopy using multiphoton-excited native fluorescence and second harmonic generation. Vol. 100, PNAS. 2003. Available from: www.pnas.orgcgidoi10.1073pnas.0832308100

32. Digman MA, Caiolfa VR, Zamai M, Gratton E. The phasor approach to fluorescence lifetime imaging analysis. Biophys J. 2008;94(2).

33. Schindelin J, Arganda-Carreras I, Frise E, Kaynig V, Longair M, Pietzsch T, et al. Fiji: An open-source platform for biological-image analysis. Vol. 9, Nature Methods. 2012.

34. Huang LK, Wang MJJ. Image thresholding by minimizing the measures of fuzziness. Pattern Recognit. 1995;28(1).

35. Crowley G, Kwon S, Caraher EJ, Haider SH, Lam R, Batra P, et al. Quantitative lung morphology: Semi-automated measurement of mean linear intercept. BMC Pulm Med. 2019;19(1).

36. Frangi AF, Niessen WJ, Vincken KL, Viergever MA. Multiscale vessel enhancement filtering. In: Lecture Notes in Computer Science (including subseries Lecture Notes in Artificial Intelligence and Lecture Notes in Bioinformatics). 1998.

37. Nejim Z, Navarro L, Morin C, Badel P. Quantitative analysis of second harmonic generated images of collagen fibers: a review. Vol. 39, Research on Biomedical Engineering. Springer Science and Business Media Deutschland GmbH; 2023. p. 273–95.

38. Otsu N. A Threshold Selection Method from Gray-Level Histograms. IEEE Trans Syst Man Cybern. 1979 Jan;9(1):62–6.

39. Roth S, Freund I. Optical second-harmonic scattering in rat-tail tendon. Biopolymers. 1981;20(6).

40. Junqueira LCU, Bignolas G, Brentani RR. Picrosirius staining plus polarization microscopy, a specific method for collagen detection in tissue sections. Histochem J. 1979;11(4).

41. Pisano ED, Zong S, Hemminger BM, Deluca M, Johnston RE, Muller K, et al. Contrast Limited Adaptive Histogram Equalization Image Processing to Improve the Detection of Simulated Spiculations in Dense Mammograms. Vol. 11, Journal of Digital Imaging. 1998.

42. Huang TS, Yang GJ, Tang GY. A Fast Two-Dimensional Median Filtering Algorithm. IEEE Trans Acoust. 1979;27(1).

43. Berezin MY, Achilefu S. Fluorescence lifetime measurements and biological imaging. Chem Rev. 2010;110(5).

44. Mereness JA, Mariani TJ. The critical role of collagen VI in lung development and chronic lung disease. Vol. 10, Matrix Biology Plus. 2021.

45. Mižíková I, Morty RE. The extracellular matrix in bronchopulmonary dysplasia: Target and source. Vol. 2, Frontiers in Medicine. 2015.

46. Kalikkot Thekkeveedu R, Guaman MC, Shivanna B. Bronchopulmonary dysplasia: A review of pathogenesis and pathophysiology. Vol. 132, Respiratory Medicine. 2017.

47. Coalson JJ. Pathology of new bronchopulmonary dysplasia. Vol. 8, Seminars in Neonatology. 2003.

48. Mižíková I, Ruiz-Camp J, Steenbock H, Madurga A, Vadász I, Herold S, et al. Collagen and elastin cross-linking is altered during aberrant late lung development associated with hyperoxia. Am J Physiol Lung Cell Mol Physiol. 2015;308(11).

49. Kumarasamy A, Schmitt I, Nave AH, Reiss I, Van Der Horst I, Dony E, et al. Lysyl oxidase activity is dysregulated during impaired alveolarization of mouse and human lungs. Am J Respir Crit Care Med. 2009;180(12).

50. Gie AG, Regin Y, Salaets T, Casiraghi C, Salomone F, Deprest J, et al. Intratracheal budesonide/surfactant attenuates hyperoxia-induced lung injury in preterm rabbits. Am J Physiol Lung Cell Mol Physiol. 2020;319(6).

51. Schittny JC. Development of the lung. Vol. 367, Cell and Tissue Research. Springer Verlag; 2017. p. 427–44.

52. Lignelli E, Palumbo F, Myti D, Morty RE. Recent advances in our understanding of the mechanisms of lung alveolarization and bronchopulmonary dysplasia. Vol. 317, American Journal of Physiology - Lung Cellular and Molecular Physiology. 2019.

53. Bhatt AJ, Pryhuber GS, Huyck H, Watkins RH, Metlay LA, Maniscalco WM. Disrupted pulmonary vasculature and decreased vascular endothelial growth factor, Flt-1, and TIE-2 in human infants dying with bronchopulmonary dysplasia. Am J Respir Crit Care Med. 2001;164(10 I).

54. De Paepe ME, Mao Q, Powell J, Rubin SE, DeKoninck P, Appel N, et al. Growth of pulmonary microvasculature in ventilated preterm infants. Am J Respir Crit Care Med. 2006;173(2).

55. Alvira CM. Aberrant pulmonary vascular growth and remodeling in bronchopulmonary dysplasia. Vol. 3, Frontiers in Medicine. 2016.

56. Azzarello F, Carli F, De Lorenzi V, Tesi M, Marchetti P, Beltram F, et al. Machine-learning-guided recognition of α and β cells from label-free infrared micrographs of living human islets of Langerhans. Sci Rep. 2024 Jun 20;14(1):14235.

57. Ranjit S, Malacrida L, Jameson DM, Gratton E. Fit-free analysis of fluorescence lifetime imaging data using the phasor approach. Nat Protoc. 2018;13(9).

58. Datta R, Alfonso-Garciá A, Cinco R, Gratton E. Fluorescence lifetime imaging of endogenous biomarker of oxidative stress. Sci Rep. 2015;5.

59. da Silva FAB, Racanelli AP, Lorand-Metze I, Metze K. Fluorescence lifetime imaging is able to recognize different hematopoietic precursors in unstained routine bone marrow films. Cytometry Part A. 2021;99(6).

Declarations

Ethical approval

All experimental procedures involving animals were approved by the local animal ethics committee and met the standard European regulations on animal research (n°783/2019-PR).

Consent for publication

Not applicable.

Availability of data and materials

All data generated or analyzed during this study are included in this published article and its supplementary information files.

Competing interests

ES, FR, GV are employees of Chiesi Farmaceutici S.p.A. XM served as a consultant for this study. The other authors have no conflicts of interest to declare.

Funding

A part of the study was funded by Chiesi Farmaceutici S.p.A. The company employees contributed to the study design, analysis, interpretation of data, and writing the manuscript.

Authors' contributions

MM, ES, FR, GV, FC conceived and planned the experiments. MM, SDM, MZ, FG, GF carried out the experiments. MM, ES, SDM, FR, GV, XM, FC contributed to the interpretation of the results. MM, ES, FR, XM, FC took the lead in writing the manuscript. All authors provided critical feedback and helped shape the research, analysis and manuscript. All authors have revised, read and approved the final manuscript.

Acknowledgments

Not applicable.